



Single-shot OCT and OCT angiography for slab-specific detection of diabetic retinopathy

GUANGRU B. LIANG,^{1,2} TRISTAN T. HORMEL,² XIANG WEI,^{1,2} YUKUN GUO,^{1,2} JIE WANG,^{1,2} THOMAS HWANG,² AND YALI JIA^{1,2,*}

¹Department of Biomedical Engineering, Oregon Health & Science University, 3303 S.W. Bond Avenue, Portland, OR 97239, USA

²Casey Eye Institute, Oregon Health & Science University, 515 S.W. Campus Drive, Portland, OR 97239, USA

*jiaya@ohsu.edu

Abstract: In this study, we present an optical coherence tomographic angiography (OCTA) prototype using a 500 kHz high-speed swept-source laser. This system can generate a 75-degree field of view with a 10.4 μm lateral resolution with a single acquisition. With this prototype we acquired detailed, wide-field, and plexus-specific images throughout the retina and choroid in eyes with diabetic retinopathy, detecting early retinal neovascularization and locating pathology within specific retinal slabs. Our device could also visualize choroidal flow and identify signs of key biomarkers in diabetic retinopathy.

© 2023 Optica Publishing Group under the terms of the [Optica Open Access Publishing Agreement](#)

1. Introduction

Diabetic retinopathy (DR) is a common microvascular complication of diabetes mellitus and a leading cause of preventable blindness [1–6]. Early detection and timely treatment of DR have been estimated to prevent 98% of the vision loss associated with the disease [7,8]. The main causes of vision loss in DR are proliferative DR (PDR), indicated by retinal neovascularization, and diabetic macular edema (DME) [8]. Originally designed for structural imaging, optical coherence tomography (OCT) is essential for diagnosing DME by providing retinal thickness measurements and detecting retinal fluid [9,10]. Its extension OCT angiography (OCTA), which became feasible due to advancements in high imaging speeds, complements OCT imaging by generating high-contrast, high-resolution angiograms, which are useful for detecting retinal neovascularization and vasculopathies [10–12].

Commercial instruments and many research OCT and OCTA devices only achieve a limited field of view (FOV). However, increasing number of reports suggests that pathological alterations in the peripheral retina shows the earliest indication of DR-related pathology [13–16]. The major challenge preventing an expanded FOV is A-scan acquisition rate. For a given A-scan rate, there is an unavoidable tradeoff between image resolution and achievable FOV [17]. This issue is exacerbated in OCTA, where two or more repeated B-scans are needed to extract the flow signal [18]. One approach is to montage several scans into an image encompassing a larger FOV [19–21]. However, montaging increases the complexity and duration of a procedure. Post-processing also becomes more difficult as individual scans need to be registered, which can introduce discontinuities.

Single-shot wide-field OCTA would overcome these limitations, but a system with such functionality would require a number of technical advances. First, image processing has several technical challenges not encountered in smaller FOV OCTA. A 2–5 ms interval between each repeated B-scan is needed to detect flow signals in the capillaries [22,23]. For large FOVs, this time interval constraint results in inevitably long acquisition times, which necessitates a motion correction technique, since blinks and passive eye movement will typically occur during imaging

[17]. Second, large FOVs introduces the challenge of iris vignetting, which usually originates from the wandering of the scanning pivot at the pupil due to the distance between the two galvo mirror scanners [24]. Third, the curvature of the retina becomes prominent in wide-field imaging, requiring a deeper imaging range.

We specifically addressed these challenges in developing a novel swept-source OCTA (SS-OCTA) prototype system that can achieve a 75-degree ($12\text{ mm} \times 23\text{-mm}$) FOV, 4 mm imaging depth, and high-resolution non-mydriatic single-shot imaging. Crucially, our wide-field 500-kHz prototype is capable of preserving capillary scale detail and is sensitive to vascular abnormalities. This is achieved through three B-scan repetitions and sensitive flow detection [25,26], motion artifact correction [27], and retinal layer segmentation [28,29]. We used this prototype SS-OCTA system to image DR patients, demonstrating its ability to detect vascular abnormalities and structural pathologies and visualize choroidal structures in the macular and peripheral regions with a single scan.

2. Methods

2.1. System overview

Our SS-OCTA system (Fig. 1) underwent a considerable design improvement from the previously reported implementation [24]. An optical relay system was employed to safely direct the laser beam through the non-dilated pupil between two galvo-mirrors in order to effectively eliminate vignetting artifacts caused by the iris. The 4f-system in our scan lens design contained two sets of achromatic lenses with effective focal lengths of 40 mm and 100 mm, respectively. The theoretical axial resolution was $5\text{ }\mu\text{m}$ in air, and the lateral resolution was $10.4\text{ }\mu\text{m}$, sufficient to achieve capillary scale resolution and isolate individual vascular plexuses throughout the image. The scan pattern used in this study was a raster scan with three repeat scans for generating OCTA images. Our definition of FOV was represented by the scan angle at the pivot in the pupil, as opposed to the alternative definition measured with respect to the eyeball center, often used in fluorescence angiography (FA) [30]. The system was compactly organized in a 3-D printed cover, and the patient interface unit was similar to a commercial OCT device (Fig. 1(C)).

2.2. 500-kHz swept-source laser

Our system uses a swept-source 500-kHz microelectromechanical systems (MEMS) vertical-cavity surface-emitting laser (VCSEL) (Thorlabs, USA). It outputs at a center wavelength of 1064 nm with a 103 nm usable optical bandwidth. Notably, the VCSEL exhibits exceptional phase stability. The standard deviation of the sweep phase velocity, calculated over 1000 A-lines, is four orders of magnitude smaller than the total phase change observed over a single sweep (Fig. 2(A)). This stability is complemented by a consistent power level characterized by an orthogonal relative intensity noise of 1.24% and an average amplified spontaneous emission contrast of 13.14%. The output power from the object lens is 2.68 mW, below the ANSI Z136.1-2013 standards for a 1064-nm constant wave laser [31]. We enabled the dual edge sampling mode of the ATS-9373 digitizer (Alazar Technologies Inc., Canada) to acquire samples at both the rising and falling edges of the frequency-varying built-in clock signal of the laser. This approach facilitated linear-in-wavenumber sampling, making the real-time OCT/OCTA display possible (see below). Because of the VCSEL's robust stability features, our system can achieve a maximum reflectance sensitivity of 107.6 dB. Signal roll-off was measured to be 3.9 dB across the entire 4 mm imaging depth (Fig. 2(B)).

2.3. GPU-based real-time display and motion-tracking software

The prototype system operates on our previously developed GPU-based data acquisition software [32]. The linear-in-wavenumber fringe acquired by the digitizer is imported from the CPU buffer

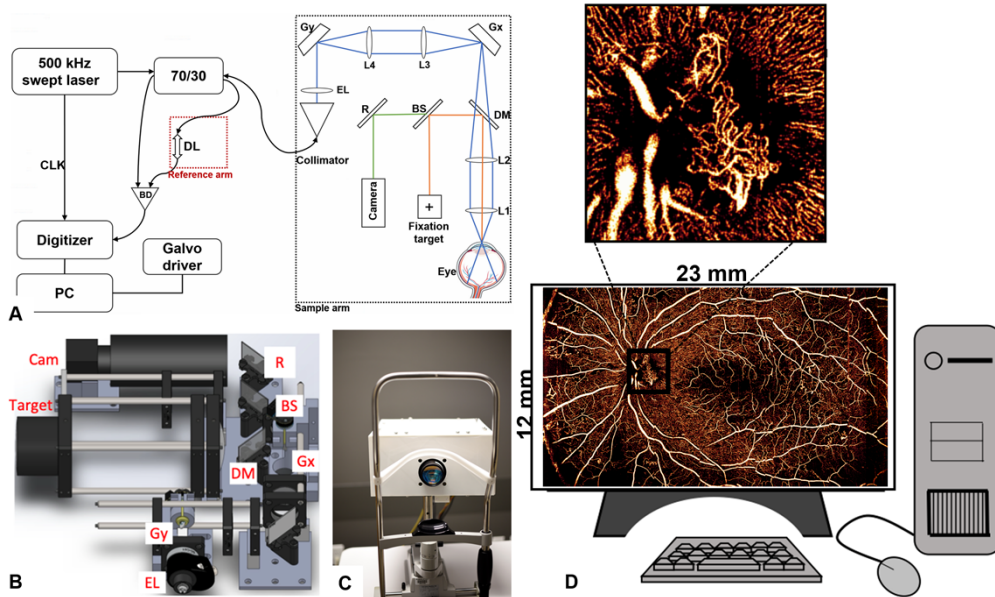


Fig. 1. System design. (A) Diagram of the wide-field OCT system; Output of the 500-kHz swept-source laser is split by a 70/30 fiber coupler, with 30% Traveling to the sample arm (dashed box). Lens groups L1 and L2 with effective focal lengths of 100 mm and 40 mm create a 4-f system that can generate a 75-degree FOV in the posterior segment. An optical relay composed of two groups of lenses (L3 and L4) is placed between the two galvo-mirrors, preventing vignetting artifacts.). The sample arm optical path also incorporates a fixation target and camera. A delay line controls the transmissive type reference arm length. The interference signal is generated and passed into a computer using a high-speed balanced photodetector and digitizer. L1: 40 mm effective focal length lens, L2: 100 mm effective focal length lens, L3 and L4: 33 mm effective focal length lenses, Gx: galvo-mirror for positioning along the x direction, Gy: galvo-mirror for positioning along the y direction, BS: beam splitter, R: silver mirror, DM: dichroic mirror, EL: electric lens, DL: delay line, BD: balanced detector, CLK: built-in sampling clock, PC: personal computer. (B) CAD rendered model (Solidworks, Dassault Systèmes). (C) Photo of the system showing its patient interface. (D) Illustration showing wide-field OCTA on a proliferative diabetic retinopathy patient being reviewed on the system's monitor. The optical design of our system enables not only the large FOV but also the single-capillary level resolution.

into the GPU cores (GeForce RTX 2080 Ti, Nvidia, USA), where digital dispersion compensation is performed before generating the structural OCT and OCTA by applying the split-spectrum amplitude-decorrelation angiography algorithm [25]. Then the reconstructed images were transferred back to the CPU buffer and displayed in the software interface (Fig. 3(A)). The real-time display can provide image quality feedback to the operator for adjusting the alignment and focus accordingly. Additionally, an efficient self-navigated motion correction method [27] can detect motion artifacts caused by blinks and microsaccades during the procedure so that the affected areas can be re-scanned (Fig. 3(B)).

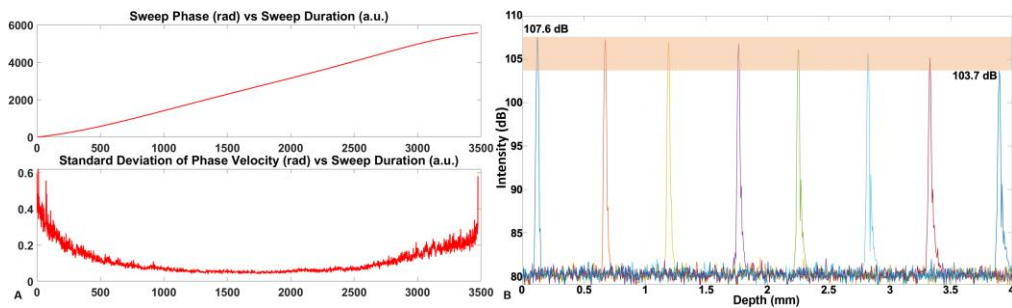


Fig. 2. Characterization of Swept-Source Laser Phase Stability and Imaging Depth Sensitivity. (A) Unwrapped sweep phase and the standard deviation of phase velocity over a single sweep of the swept-source laser. Both curves are plotted in radians on the Y-axis, while the X-axis uses the same arbitrary unit (a.u.). The standard deviation of the phase velocity, calculated over 1000 A-lines, is four orders of magnitude smaller than the total phase change observed over a whole sweep, emphasizing the high stability of the laser sweep phase. (B) Reflectance sensitivity roll-off across imaging depth. The Different colors represent different depths. The beige-shaded rectangle represents the signal roll-off from the shallowest to the deepest location. The high overall reflectance sensitivity and extended imaging depth enable high quality images of the retina and choroidal in wide-field imaging.

2.4. System performance and technical specifications

Our system achieves a maximum scanning FOV of 38 degrees (fast axis) \times 75 degrees (slow axis), equivalent to a 12 \times 23-mm area in the human eye with a standard 23 mm axial length. The generated volumetric data encompasses 1536 pixels per A-line, 1208 A-lines per B-scan, and a total of 2304 B-scans. This corresponds to a sampling density of 10 $\mu\text{m}/\text{pixel}$, providing a high-resolution depiction of retinal features. A complete wide-field scan takes approximately 16.6 seconds if no rescan is triggered by eye motion. Based on the experience of our operator, the average scan time is around 21 seconds with rescans, but this obviously varies depending on the number of rescans required. The additional time accommodates microsaccades and the patient's freedom to blink naturally during the scanning process, serving to relieve eye fatigue while still preserving image quality through triggered rescans. If procedure times become prohibitive, we can turn off our motion correction system and remove many artifacts, though not all, with image processing.

2.5. Recruitment and imaging procedures

93 DR patients were recruited from the retina clinic of the Casey Eye Institute. Volunteers underwent a thorough medical history inquiry, comprehensive clinical examinations, and ocular imaging, which included fundus photography and 6 \times 6-mm OCTA volumetric scans. Retina specialists diagnosed the various stages of DR. Before enrollment, participants provided written informed consent. The study received approval from the Institutional Review Board of Oregon Health & Science University, ensuring adherence to all tenets of the Declaration of Helsinki.

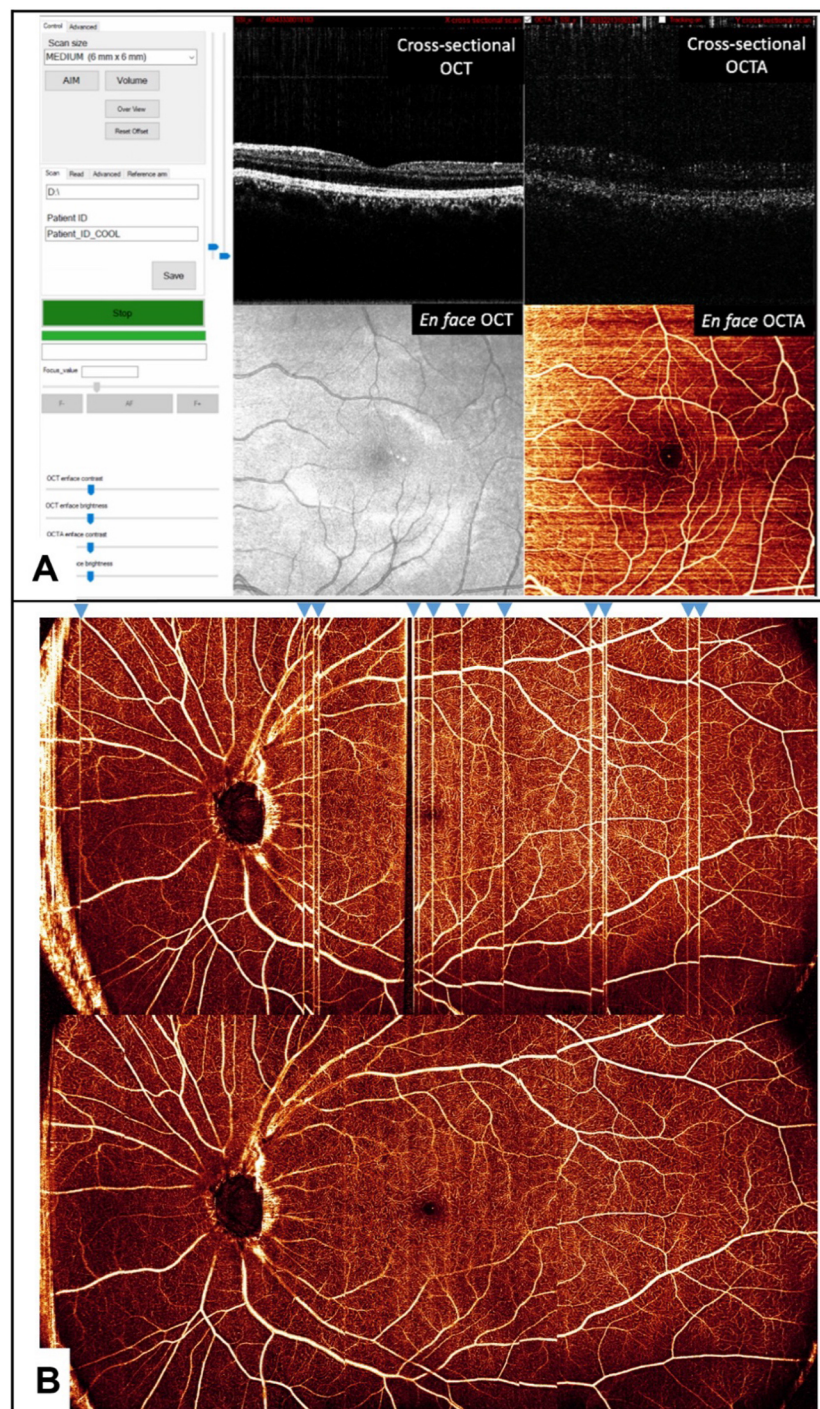


Fig. 3. (A) The system user interface guided by real-time cross-sectional and *en face* OCT/OCTA. (B) Demonstration of motion correction using the self-tracking algorithm: the motion-tracking is off during the acquisition of the top image and is on when acquiring the bottom image; Blue arrows on the top indicate the presence of motion artifacts, significantly reduced on the bottom image.

3. Results

3.1. Imaging of plexus-specific vascular pathologies

Using the high-resolution and large-FOV capabilities of our system, we were able to identify both central and peripheral pathologies in representative wide-field OCTA images from a PDR patient (Fig. 4). These include retinal neovascularization (RNV), microaneurysms, and intraretinal microvascular abnormalities (IRMA) in the superficial vascular complex (SVC) (Fig. 4(A)).

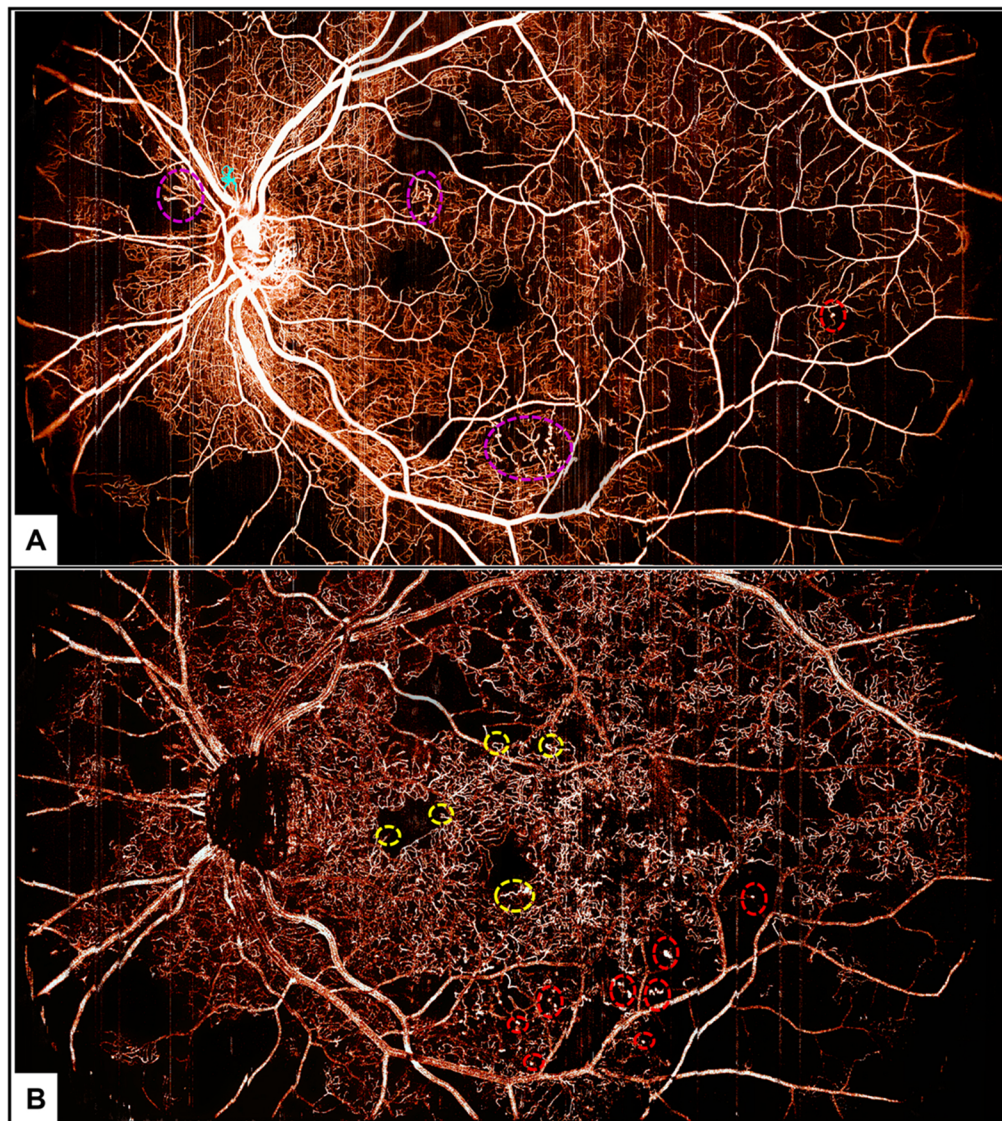


Fig. 4. 75-degree wide-field OCTA images of an eye with proliferative diabetic retinopathy. (A) SVC *en face* projection exhibiting retinal neovascularization (highlighted in cyan), intraretinal microvascular abnormalities (purple circles), and a microaneurysm (red). (B) *En face* projection of the DVC, showing numerous microaneurysms (red) and dilated vessels (yellow). These pathologies can be observed in a panoramic FOV captured with our single-shot system.

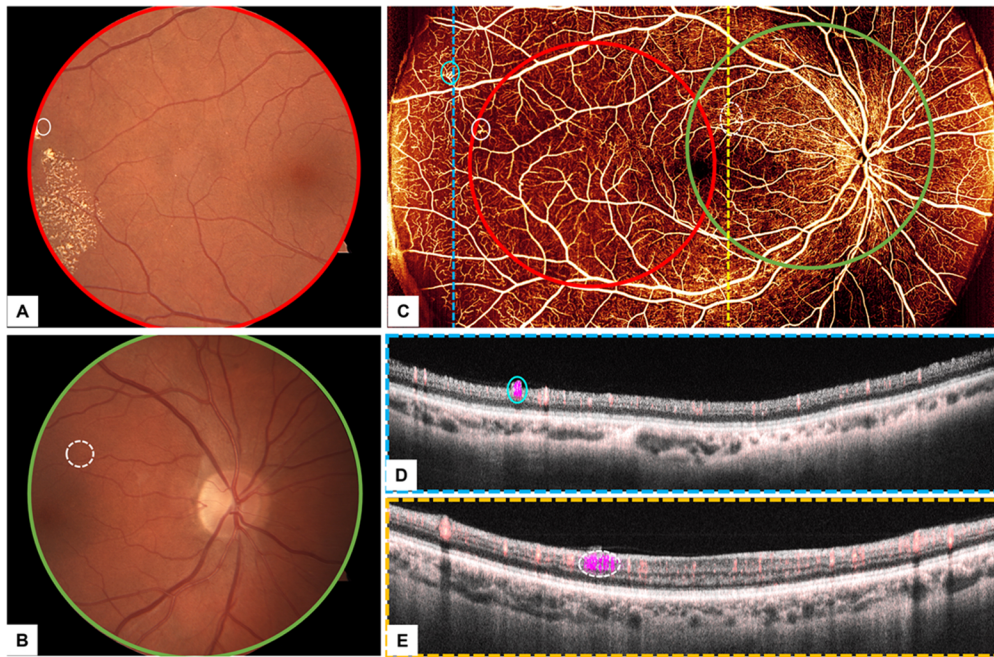


Fig. 5. Subclinical feature detection. (A) Fundus photo of the macula. (B) Fundus photo of the disc. (C) Wide-field *en face* OCTA of the superficial vascular complex, covering the same area as A (red circle) and B (green circle). A proliferative vessel (cyan circle) and two IRMAs (white circles) were captured by the prototype, but they are either outside of the FOV or not obvious in fundus photos. (D) Cross-sectional OCTA overlaid on structural OCT at the position of the blue dashed line in (C), showing RNV (cyan circle). (E) Cross-sectional OCTA overlaid on structural OCT at the position of the yellow dashed line in (C), showing IRMA (white dashed circle).

Moreover, numerous microaneurysms and dilated vessels in the deep vascular complex (DVC) are perceptible from the same patient (Fig. 4(B)).

3.2. Retinal neovascularization (RNV) and precursors

In an eye diagnosed with moderate nonproliferative DR, no RNV was detected with fundus photography (Fig. 5 (A, B)) (FF450, Carl Zeiss Meditec AG, Jena, Germany). However, our prototype visualized signs of the earliest form of RNV in the periphery of the SVC (Fig. 5 (C, D)), which is also known as the RNV sprout [33]. Therefore, the eye was likely progressing into proliferative DR. The vascular details, including IRMAs, appear with greater clarity in the prototype OCTA image (Fig. 5(C)), compared to those in fundus photos (Fig. 5(A, B)), which failed to detect IRMAs in the same spot as shown in the OCTA image.

3.3. High-resolution structural OCT of slab-specific pathologies

High lateral and axial resolutions also allow this prototype to detect structural pathologies in different retinal anatomical layers, such as epiretinal membranes (ERM), photoreceptor disruption, and macular edema (Fig. 6), all of which can contribute to poor visual outcomes [34–39]. The OCT structural images reveal individual nerve fibers and their distribution, including the characteristic Raphe in the nerve fiber layer (Fig. 6(A)). Additionally, signs of ERM are also observable (Fig. 6(B)). In the images from a second patient, the inner and outer segments of the photoreceptor display areas of photoreceptor disruption, while the cross-sectional image

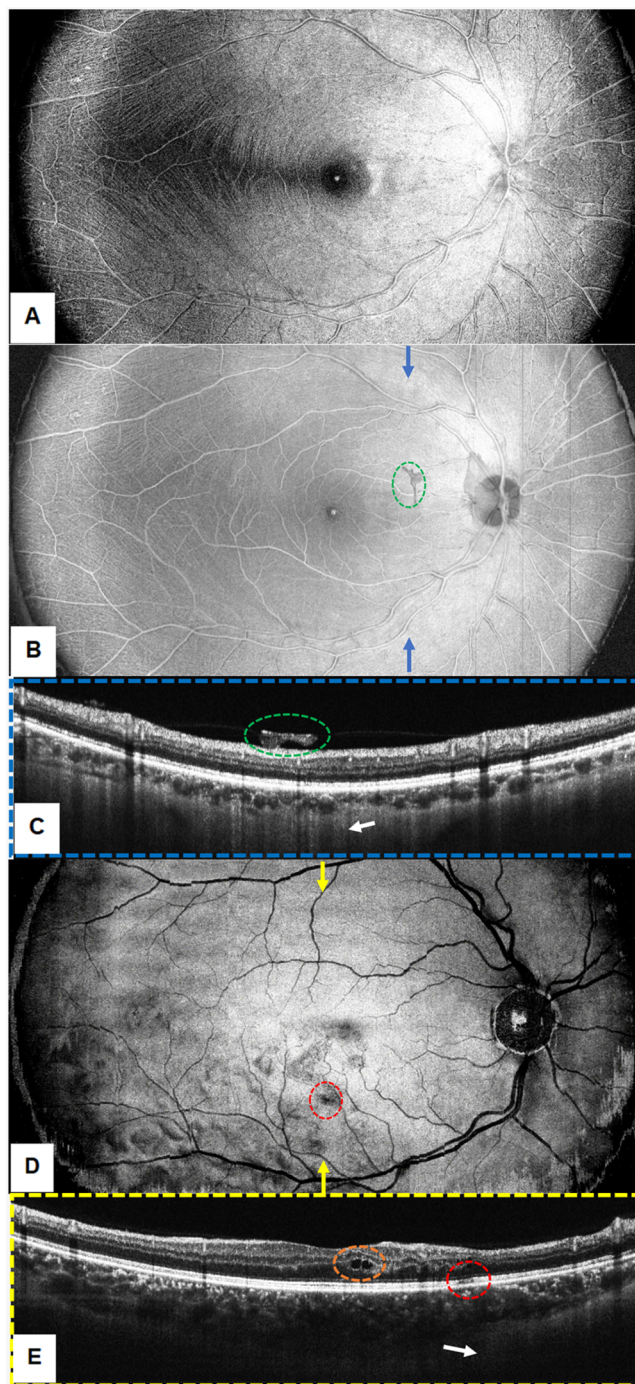


Fig. 6. High-resolution wide-field OCT structural images from DR patients. (A) *En face* projection of the nerve fiber layer showing individual nerve fibers. (B) Inner limiting membrane showing signs of epiretinal membrane (ERM) (green dashed circle). (C) OCT cross-section at the plane marked by blue arrows in (B), also showing features of ERM (green dashed circle). (D) The inner and outer segments exhibit photoreceptor disruption (red dashed circle). (E) OCT cross-section at the plane marked by yellow arrows in (D), showing intra-retinal fluid (orange circle) and photoreceptor disruption (red dashed circle).

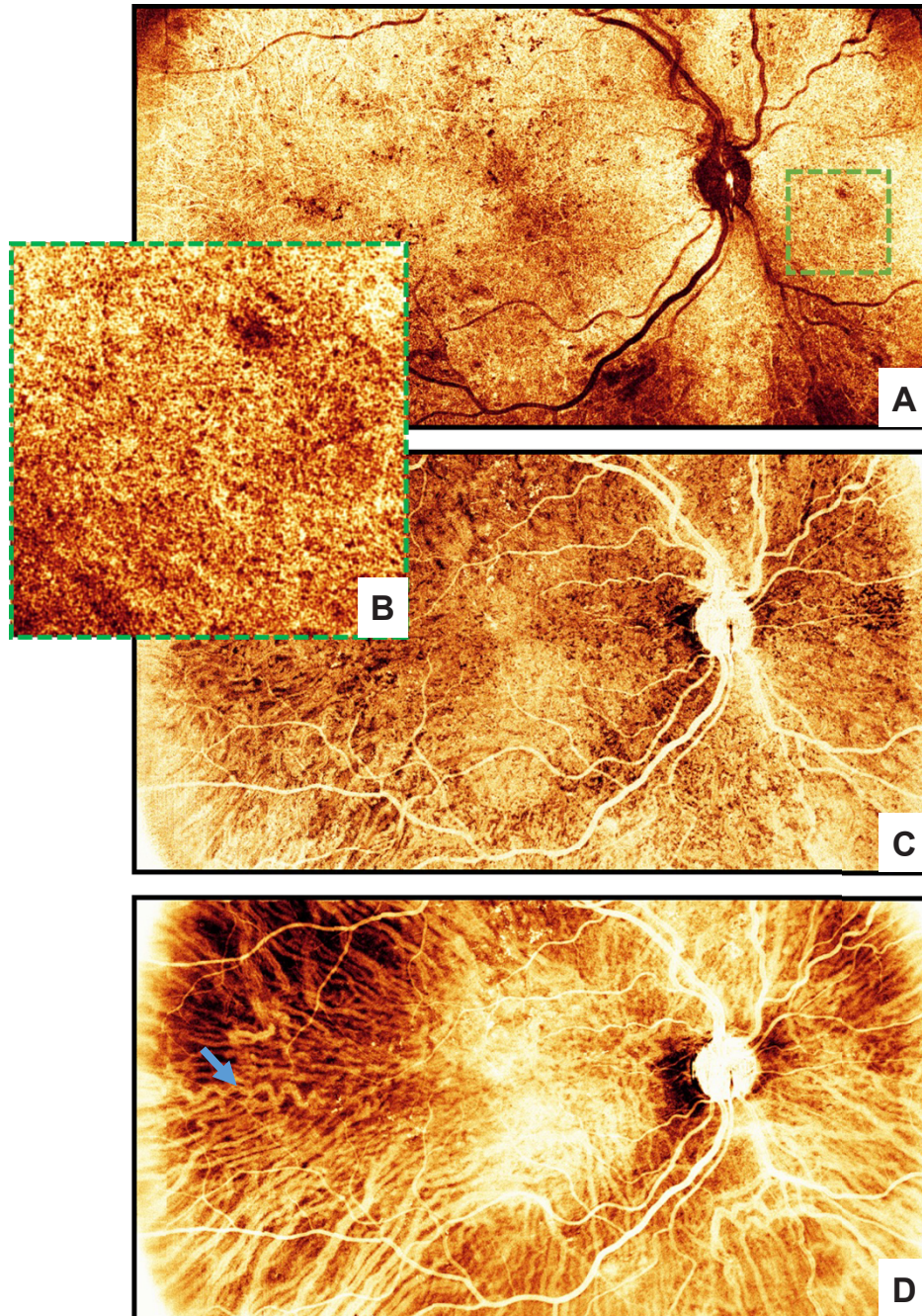


Fig. 7. Choroidal *en face* projections from a proliferative diabetic retinopathy patient. (A) Choriocapillaris. (B) Enlarged areas marked in (A), showing detailed choriocapillaris with fenestrated nature. (C) Inverse OCT projection of Sattler's layer. (D) Inverse OCT projection of Haller's layer, with a tortuous vessel captured in the temporal region indicated by the blue arrow. The system demonstrates the capability to image choroidal vascular structures.

indicates the location of intra-retinal fluid (Fig. 6(C)). The high-SNR images also allow for the visualization of the posterior boundary of the choroid in the cross-sectional B-scan images.

3.4. Deep tissue penetration for visualizing choroidal vessels

Choroidal vascular changes are predictors of DR progression [40–42]. However, imaging the choroid with a conventional OCT instrument can be difficult even for an experienced operator due to limited tissue penetration and resolution. In this representative case with PDR, our system successfully obtained detailed *en face* projections of the choriocapillaris, Sattler's layer, and Haller's layer (Fig. 7) facilitated by the high resolution, penetration depth, and reflectance sensitivity of the system. The choriocapillaris exhibited clear fenestrations (Fig. 7(A), (B)), consistent with its histological appearance as a network of fine capillaries [41]. Imaging of Sattler's layer (Fig. 7(C)) and Haller's layers (Fig. 7(D)) reveals the architecture of the medium to large-size blood vessels which play critical roles in the choroid's blood supply, including a particularly notable tortuous vessel in the temporal region in the Haller's layers. These detailed observations of the choroidal vasculature, encompassing all three layers and specific morphological features, have never before been demonstrated within a single-acquisition.

4. Discussion

While OCT and OCTA combined have many advantages over the traditional retinal imaging modalities, a key disadvantage in contemporary commercial instruments and many research devices is a small FOV. Since the earliest signs of DR development tend to appear in the peripheral region of the retina [13–15], small fields of view can be considered a primary weakness of OCT/OCTA, if not its most important. In addition, new studies also suggest that choroidal circulation alteration, such as choriocapillaris loss [41], loss of large blood vessels in the Sattler's layer and Haller's layers [40], decrease in choroidal flow [43], or reduced choroidal thickness [42] are implicated in DR. However, like peripheral pathology, conventional OCT devices cannot adequately evaluate choroidal features due to the limited lateral resolution for choriocapillaris and the lack of deeper tissue penetration [40].

We addressed these concerns by achieving a single-shot wide-field OCTA system with a 75-degree FOV and 10.4 μm lateral resolution. To the best of our knowledge, high-resolution OCTA prototypes with FOV larger than 60 degrees have only previously been achieved through montage [19–21]. In our system, we instead took advantage of a high-speed swept-source laser to increase the total number of A-lines sampled, thereby increasing the FOV without losing resolution or imposing excessive procedure times. We also incorporated other techniques, including motion correction with a self-navigated algorithm [27], an optical relay between the two galvo-mirrors to route the laser beam safely through the non-dilated pupil to avoid vignetting artifacts [24], and a swept laser and digitizer setup capable of achieving a total imaging depth of 4 mm and a sensitivity of >100 dB at the deepest points in the imaging range.

All of these capabilities could help improve clinical outcomes for DR and be used to explore DR pathophysiology. First, by enabling the simultaneous detection of macular, peripapillary, and peripheral pathology, our device can deliver a more comprehensive assessment of DR pathogenesis. This includes early indicators of developing RNV, such as retinal neovascular sprouts [34,44], along with the ability to detect and monitor IRMAs and microaneurysms, two of the key biomarkers in the progression of DR. The pathology detection capabilities of our device stand in contrast to contemporary commercial devices, which struggle to correlate peripheral and centrally located pathologic features (as in the case of OCT and OCTA), associate pathologic features between different retinal depths (as with fundus photography or dye-based angiography), or reveal capillary-scale vascular disruptions throughout the retina and choroid. But correlations between pathologic features and the extent to which they can predict future pathologic development are essential information in therapeutic research because they can inform

clinical trial endpoints and indicate treatment efficacy [45]. Devices following our method could therefore generate insights for therapy development.

Second, single-shot imaging provides a foundation from which disease characteristics can be explored with enough data to make statistically meaningful insights. While montaging several OCT/OCTA volumes to produce wide-field imaging can reveal similar pathologic features to those examined in this work, the approach may not be clinically practical. Capturing multiple volumes extends procedure time and complexity. In turn, exorbitant procedure requirements can ultimately reduce the quantity of data available for analysis due to patient fatigue and the need to train technicians to perform complex tasks. Together these shortcomings can prevent efficient development and testing of image processing algorithms (particularly those that rely on machine learning approaches [46], which require large datasets for training).

Finally, wide-field single-shot OCT/OCTA imaging has far-reaching potential as a screening technology. The non-invasive, simple, and cost-effective procedures provide a comprehensive analysis of DR-related pathology, thus improving patient stratification. The combination of high resolution and large FOV of this technology is essential in detecting early signs of DR, such as microaneurysms, IRMA, and RNV. Furthermore, without compromising sensitivity, OCTA is faster, safer, and less expensive than FA, thereby positioning it as a more suitable choice for routine DR screening.

Although our prototype has shown its reliability for imaging DR pathology, further improvements can be considered. Firstly, we enabled the dual edge sampling mode of our digitizer to double the k-clock sampling points; however, the k-clock is at a very high frequency (close to 1 GHz), and the timing jitter (small variations in the expected timing of the clock signal) become a significant issue, leading to reduced SNR and spectral leakage. An alternative internal clock mode [47,48] could achieve high stability by computing the instantaneous phase of the laser sweep from the interference fringe of a calibrated Mach-Zehnder interferometer (MZI). This could further improve the SNR and imaging depth in our system. Secondly, the MEMS-VCSEL laser we used can enable a bi-directional sweep which could achieve a 1-MHz sweep rate with a 100% duty cycle. However, the up and down sweeps will have different sweep phase versus time behavior, which will cause asymmetries between adjacent A-lines without proper phase calibration [47]. The calibration of these sweep phase asymmetries can be explored in the future. In the context of laser costs, it's relevant to note that while the use of a swept-source laser in our prototype does present a higher financial barrier due to its market price of approximately \$40 k, this is likely to change. Prices for swept-source lasers are on a downward trend, and emerging commercial devices have begun to incorporate them, indicating a pathway toward broader, more cost-effective utilization. Thirdly, the sampling density of our 75-degree scanning is still below the Nyquist limit. This could be corrected with a faster A-scan rate (by enabling the 1-MHz mode) and a refined motion correction algorithm. Additionally, it's worth noting that the actual lateral resolution of our system is subject to waveform aberrations. These aberrations, predominantly influenced by the optical properties of the patient's eye, are particularly pronounced in peripheral regions and lead to inconsistent lateral resolution across the FOV. Future works focusing on refined optics design could serve to minimize such effects. Lastly, retinal layer segmentation algorithms are not optimized for wide-field OCT/OCTA images [28,29]. Future work on such optimization should be attempted to make our approach more practical, considering that layer segmentation is among the most time-consuming tasks in OCTA image processing.

5. Conclusion

We demonstrated a prototype that can achieve high-resolution single-volume 75-degree FOV OCTA retinal and choroidal imaging that has been optimized for slab-specific DR analysis. The system utilizes a high SNR 500-kHz MEMS-VCSEL laser and integrates an efficient motion correction algorithm in a GPU-based real-time acquisition software. We can capture wide-field

images with both vascular and structural pathologies in different DR severities, and clear retinal and choroidal details can be observed. This study presents a powerful tool for DR diagnostics and research.

Funding. National Institutes of Health (P30 EY010572, R01 EY024544, R01 EY027833, R01 EY031394, R01 EY035410, T32 EY023211, UL1TR002369); MD Endowed Fund for Innovation (the Malcolm M. Marquis); Oregon Health and Science University (Departmental Funding Grant); Research to Prevent Blindness (Dr. H. James and Carole Free Catalyst Award); Edward N. and Della L. Thome Memorial Foundation; Bright Focus Foundation (G2020168, M20230081).

Disclosures. Oregon Health & Science University (OHSU), Dr. Yali Jia, Dr. Jie Wang, and Mr. Yukun Guo have a significant financial interest in Optovue/Visionix, Inc. and Genentech, Inc.; OHSU and Dr. Jia also have a significant financial interest in Optos, Inc. These potential conflicts of interest have been reviewed and managed by OHSU. Other authors declare no conflicts of interest related to this article.

Data availability. Data underlying the results presented in this paper are not publicly available at this time but may be obtained from the authors upon reasonable request.

References

1. Z. L. Teo, Y. C. Tham, M. Yu, M. L. Chee, T. H. Rim, N. Cheung, M. M. Bikbov, Y. X. Wang, Y. Tang, Y. Lu, I. Y. Wong, D. S. W. Ting, G. S. W. Tan, J. B. Jonas, C. Sabanayagam, T. Y. Wong, and C. Y. Cheng, "Global Prevalence of Diabetic Retinopathy and Projection of Burden through 2045: Systematic Review and Meta-analysis," *Ophthalmology* **128**(11), 1580–1591 (2021).
2. H. Khalil, "Diabetes microvascular complications—A clinical update," *Diabetes & Metabolic Syndrome: Clinical Research & Reviews* **11**, S133–S139 (2017).
3. L. S. Lim, G. Liew, N. Cheung, P. Mitchell, and T. Y. Wong, "Mixed messages on systemic therapies for diabetic retinopathy," *The Lancet* **376**(9751), 1461 (2010).
4. S. Sivaprasad, B. Gupta, R. Crosby-Nwaobi, and J. Evans, "Prevalence of Diabetic Retinopathy in Various Ethnic Groups: A Worldwide Perspective," *Surv Ophthalmol* **57**(4), 347–370 (2012).
5. D. S. Fong, L. Aiello, T. W. Gardner, G. L. King, G. Blankenship, J. D. Cavallerano, F. L. Ferris, and R. Klein, "Retinopathy in Diabetes," *Diabetes Care* **27**(suppl_1), s84–s87 (2004).
6. N. G. Congdon, D. S. Friedman, and T. Lietman, "Important Causes of Visual Impairment in the World Today," *JAMA* **290**(15), 2057–2060 (2003).
7. T. Y. Wong, J. Sun, R. Kawasaki, P. Ruamviboonsuk, N. Gupta, V. C. Lansingh, M. Maia, W. Mathenge, S. Moreker, M. M. K. Muqit, S. Resnikoff, J. Verdaguer, P. Zhao, F. Ferris, L. P. Aiello, and H. R. Taylor, "Guidelines on Diabetic Eye Care: The International Council of Ophthalmology Recommendations for Screening, Follow-up, Referral, and Treatment Based on Resource Settings," *Ophthalmology* **125**(10), 1608–1622 (2018).
8. C. J. Flaxel, R. A. Adelman, S. T. Bailey, A. Fawzi, J. I. Lim, G. A. Vemulakonda, and G. Ying, "Diabetic Retinopathy Preferred Practice Pattern®," *Ophthalmology* **127**(1), P66–P145 (2020).
9. Y. Guo, T. T. Hormel, H. Xiong, J. Wang, T. S. Hwang, and Y. Jia, "Automated Segmentation of Retinal Fluid Volumes From Structural and Angiographic Optical Coherence Tomography Using Deep Learning," *Transl Vis Sci Technol* **9**(2), 54 (2020).
10. Q. S. You, K. Tsuboi, Y. Guo, J. Wang, C. J. Flaxel, S. T. Bailey, D. Huang, Y. Jia, and T. S. Hwang, "Comparison of Central Macular Fluid Volume With Central Subfield Thickness in Patients With Diabetic Macular Edema Using Optical Coherence Tomography Angiography," *JAMA Ophthalmol* **139**(7), 734–741 (2021).
11. J. F. Russell, H. W. Flynn, J. Sridhar, J. H. Townsend, Y. Shi, K. C. Fan, N. L. Scott, J. W. Hinkle, C. Lyu, G. Gregori, S. R. Russell, and P. J. Rosenfeld, "Distribution of Diabetic Neovascularization on Ultra-Widefield Fluorescein Angiography and on Simulated Widefield OCT Angiography," *Am J Ophthalmol* **207**, 110–120 (2019).
12. V. Schreur, A. Domanian, B. Liefers, F. G. Venhuizen, B. J. Klevering, C. B. Hoyng, E. K. de Jong, and T. Theelen, "Morphological and topographical appearance of microaneurysms on optical coherence tomography angiography," *Br J Ophthalmol.* **103**(5), 630–635 (2019).
13. K. Ghasemi Falavarjani, I. Tsui, and S. R. Sadda, "Ultra-wide-field imaging in diabetic retinopathy," *Vision Res* **139**, 187–190 (2017).
14. P. S. Silva, A. J. Dela Cruz, M. G. Ledesma, J. van Hemert, A. Radwan, J. D. Cavallerano, L. M. Aiello, J. K. Sun, and L. P. Aiello, "Diabetic Retinopathy Severity and Peripheral Lesions Are Associated with Nonperfusion on Ultrawide Field Angiography," *Ophthalmology* **122**(12), 2465–2472 (2015).
15. P. S. Silva, J. D. Cavallerano, N. M. N. Haddad, H. Kwak, K. H. Dyer, A. F. Omar, H. Shikari, L. M. Aiello, J. K. Sun, and L. P. Aiello, "Peripheral Lesions Identified on Ultrawide Field Imaging Predict Increased Risk of Diabetic Retinopathy Progression over 4 Years," *Ophthalmology* **122**(5), 949–956 (2015).
16. T. T. Hormel and Y. Jia, "OCT angiography and its retinal biomarkers [Invited]," *Biomed. Opt. Express* **14**(9), 4542 (2023).
17. R. F. Spaide, J. G. Fujimoto, and N. K. Waheed, "Image Artifacts in Optical Coherence Angiography," *Retina* **35**(11), 2163–2180 (2015).

18. S. Makita, Y. Hong, M. Yamanari, T. Yatagai, and Y. Yasuno, "Optical coherence angiography," *Opt. Express* **14**(17), 7821–7840 (2006).
19. F. P. Wang, S. S. Saraf, Q. Zhang, R. K. Wang, and K. A. Rezaei, "Ultra-Widefield Protocol Enhances Automated Classification of Diabetic Retinopathy Severity with OCT Angiography," *Ophthalmol Retina* **4**(4), 415–424 (2020).
20. J. Wang, A. Camino, X. Hua, L. Liu, D. Huang, T. S. Hwang, and Y. Jia, "Invariant features-based automated registration and montage for wide-field OCT angiography," *Biomed. Opt. Express* **10**(1), 120–136 (2019).
21. M. Niederleithner, L. de Sisternes, H. Stino, A. Sedova, T. Schlegl, H. Bagherinia, A. Britten, P. Matten, U. Schmidt-Erfurth, A. Pollreisz, W. Drexler, R. A. Leitgeb, and T. Schmoll, "Ultra-widefield OCT Angiography," *IEEE Trans Med Imaging* **42**(4), 1009–1020 (2023).
22. W. Choi, E. M. Moult, N. K. Waheed, M. Adhi, B. Lee, C. D. Lu, T. E. de Carlo, V. Jayaraman, P. J. Rosenfeld, J. S. Duker, and J. G. Fujimoto, "Ultrahigh-Speed, Swept-Source Optical Coherence Tomography Angiography in Nonexudative Age-Related Macular Degeneration with Geographic Atrophy," *Ophthalmology* **122**(12), 2532–2544 (2015).
23. X. Wei, T. T. Hormel, S. Pi, Y. Jian, Y. Guo, and Y. Jia, "High dynamic range optical coherence tomography angiography (HDR-OCTA)," *Biomed. Opt. Express* **10**(7), 3560–3571 (2019).
24. X. Wei, T. T. Hormel, Y. Guo, and Y. Jia, "75-degree non-mydratic single-volume optical coherence tomographic angiography," *Biomed. Opt. Express* **10**(12), 6286–6295 (2019).
25. Y. Jia, O. Tan, J. Tokayer, B. Potsaid, Y. Wang, J. J. Liu, M. F. Kraus, H. Subhash, J. G. Fujimoto, J. Horngger, and D. Huang, "Split-spectrum amplitude-decorrelation angiography with optical coherence tomography," *Opt. Express* **20**(4), 4710 (2012).
26. J. P. Su, R. Chandwani, S. S. Gao, A. D. Pechauer, M. Zhang, J. Wang, Y. Jia, D. Huang, and G. Liu, "Calibration of optical coherence tomography angiography with a microfluidic chip," *J. Biomed. Opt.* **21**(08), 1 (2016).
27. X. Wei, T. T. Hormel, Y. Guo, T. S. Hwang, and Y. Jia, "High-resolution wide-field OCT angiography with a self-navigation method to correct microsaccades and blinks," *Biomed. Opt. Express* **11**(6), 3234 (2020).
28. Y. Guo, T. T. Hormel, S. Pi, X. Wei, X. Wei, M. Gao, J. C. Morrison, and Y. Jia, "An end-to-end network for segmenting the vasculature of three retinal capillary plexuses from OCT angiographic volumes," *Biomed. Opt. Express* **12**(8), 4889–4900 (2021).
29. Y. Guo, A. Camino, M. Zhang, J. Wang, D. Huang, T. Hwang, and Y. Jia, "Automated segmentation of retinal layer boundaries and capillary plexuses in wide-field optical coherence tomographic angiography," *Biomed. Opt. Express* **9**(9), 4429–4442 (2018).
30. J. Mao, Y. Shao, J. Lao, X. Yu, Y. Chen, C. Zhang, H. Li, and L. Shen, "Ultra-wide-field imaging and intravenous fundus fluorescein angiography in infants with retinopathy of prematurity," *Retina* **40**(12), 2357–2365 (2020).
31. American National Standard Institute, American National Standard for Safe Use of Lasers (ANSI Z136.1-2014) (2014).
32. X. Wei, A. Camino, S. Pi, T. T. Hormel, W. Cepurna, D. Huang, J. C. Morrison, and Y. Jia, "Real-time cross-sectional and en face OCT angiography guiding high-quality scan acquisition," *Opt. Lett.* **44**(6), 1431 (2019).
33. K. Tsuboi, Y. Ishida, T. Wakabayashi, and M. Kamei, "Presumed Glial Sprouts as a Predictor of Preretinal Neovascularization in Retinal Vein Occlusion," *JAMA Ophthalmol* **140**(3), 284–285 (2022).
34. S. F. Oster, F. Mojana, M. Brar, R. M. S. Yuson, L. Cheng, and W. R. Freeman, "Disruption of the photoreceptor inner segment/outer segment layer on spectral domain-optical coherence tomography is a predictor of poor visual acuity in patients with epiretinal membranes," *Retina* **30**(5), 713–718 (2010).
35. L. M. E. Scheerlinck, R. van der Valk, and R. van Leeuwen, "Predictive factors for postoperative visual acuity in idiopathic epiretinal membrane: a systematic review," *Acta Ophthalmol* **93**(3), 203–212 (2015).
36. H. J. Shin, S. H. Lee, H. Chung, and H. C. Kim, "Association between photoreceptor integrity and visual outcome in diabetic macular edema," *Graefes Arch Clin. Exp. Ophthalmol.* **250**(1), 61–70 (2012).
37. A. S. Maheshwary, S. F. Oster, R. M. S. Yuson, L. Cheng, F. Mojana, and W. R. Freeman, "The association between percent disruption of the photoreceptor inner segment-outer segment junction and visual acuity in diabetic macular edema," *Am J Ophthalmol* **150**(1), 63–67.e1 (2010).
38. Z. Wang, A. Camino, M. Zhang, J. Wang, T. S. Hwang, Z. Wang, D. J. Wilson, D. Huang, D. Li, and Y. Jia, "Automated detection of photoreceptor disruption in mild diabetic retinopathy on volumetric optical coherence tomography," *Biomed. Opt. Express* **8**(12), 5384–5398 (2017).
39. A. Uji, T. Murakami, N. Unoki, K. Ogino, T. Horii, S. Yoshitake, Y. Dodo, and N. Yoshimura, "Parallelism for quantitative image analysis of photoreceptor-retinal pigment epithelium complex alterations in diabetic macular edema," *Invest. Ophthalmol. Visual Sci.* **55**(5), 3361–3367 (2014).
40. D. Ferrara, N. K. Waheed, and J. S. Duker, "Investigating the choriocapillaris and choroidal vasculature with new optical coherence tomography technologies," *Prog Retin Eye Res* **52**, 130–155 (2016).
41. J. Cao, D. S. McLeod, C. A. Merges, and G. A. Lutty, "Choriocapillaris Degeneration and Related Pathologic Changes in Human Diabetic Eyes," *Arch. Ophthalmol.* **116**(5), 589–597 (1998).
42. C. Gupta, R. Tan, C. Mishra, N. Khandelwal, R. Raman, R. Kim, R. Agrawal, and P. Sen, "Choroidal structural analysis in eyes with diabetic retinopathy and diabetic macular edema—A novel OCT based imaging biomarker," *PLoS One* **13**(12), e0207435 (2018).

43. T. Nagaoka, N. Kitaya, R. Sugawara, H. Yokota, F. Mori, T. Hikichi, N. Fujio, and A. Yoshida, "Alteration of choroidal circulation in the foveal region in patients with type 2 diabetes," *Br. J. Ophthalmol.* **88**(8), 1060–1063 (2004).
44. K. Tsuboi, M. Mazloumi, Y. Guo, J. Wang, C. J. Flaxel, S. T. Bailey, D. Huang, Y. Jia, and T. S. Hwang, "Utility of En Face OCT for the Detection of Clinically Unsuspected Retinal Neovascularization in Patients with Diabetic Retinopathy," *Ophthalmol Retina* **7**(8), 683–691 (2023).
45. J. Lechner, O. E. O'Leary, and A. W. Stitt, "The pathology associated with diabetic retinopathy," *Vision Res* **139**, 7–14 (2017).
46. T. T. Hormel, T. S. Hwang, S. T. Bailey, D. J. Wilson, D. Huang, and Y. Jia, "Artificial intelligence in OCT angiography," *Prog Retin Eye Res* **85**, 100965 (2021).
47. J. Zhang, T. Nguyen, B. Potsaid, V. Jayaraman, C. Burgner, S. Chen, J. Li, K. Liang, A. Cable, G. Traverso, H. Mashimo, and J. G. Fujimoto, "Multi-MHz MEMS-VCSEL swept-source optical coherence tomography for endoscopic structural and angiographic imaging with miniaturized brushless motor probes," *Biomed. Opt. Express* **12**(4), 2384 (2021).
48. S. Chen, B. Potsaid, Y. Li, J. Lin, Y. Hwang, E. M. Moult, J. Zhang, D. Huang, and J. G. Fujimoto, "High speed, long range, deep penetration swept source OCT for structural and angiographic imaging of the anterior eye," *Sci. Rep.* **12**(1), 992 (2022).